

Dynamics, Aggregation, and Interfacial Properties of the Partially Hydrolyzed Polyacrylamide Polymer for Enhanced Oil Recovery Applications: Insights from Molecular Dynamics Simulations

Safwat Abdel-Azeim*[✉] and Mazen Y. Kanj

Center for Integrative Petroleum Research (CIPR), College of Petroleum Engineering and Geosciences, King Fahd University of Petroleum and Minerals (KFUPM), Dhahran 31261, Saudi Arabia

S Supporting Information

ABSTRACT: We hereby employ molecular dynamics (MD) simulations ($\sim 6 \mu\text{s}$ in total) to investigate the chain dynamics, aggregation, and interfacial properties of the partially hydrolyzed polyacrylamide (HPAM) polymer. HPAM is widely used in chemical enhanced oil recovery (cEOR) applications. The conformational changes and aggregation properties are examined in different conditions simulating cEOR activities. Also, we examined the degree of polymerization (20-, 50-, and 100 -mers) effect on the polymer chain dynamics and aggregation. MD simulations showed that HPAM has a high conformational diversity ranging from coiled to compact conformations. The former is abundantly found in fresh water. In brine solutions, HPAM is found to be very sensitive to ions and adopts a more compact conformation. HPAM-ion interactions drive the conformational thermodynamic equilibrium between the compact and coiled conformations toward the compact conformation. Furthermore, ion interactions are largely impacting its aggregation. HPAM has a high propensity to form large-size aggregates in brine solution. An interesting ionic effect has been observed; Ca^{2+} ions showed a high affinity toward HPAM compared to Mg^{2+} and Na^+ ions. The electrostatic forces and ionic dehydration free energy penalty are the two main factors that determine the HPAM ionic affinity. Short oligomers are noted to overestimate the tendency of the polymer to have compact conformations and underestimate its aggregation capacity in brine solutions. Simulations of oil–water systems show that HPAM has a spectator role on the interfacial tension in the absence of surfactants.

INTRODUCTION

The primary and secondary oil recovery methods are able to only extract 30–40% of the original oil in place.^{1,2} As such, a large amount of this oil remains untapped.³ It is vital to develop tertiary recovery [or enhanced oil recovery (EOR)] techniques to extract the residual oil and meet the increasing global energy demand.^{4–6} One widely used EOR method is the chemical enhanced oil recovery (cEOR).^{7–10} The partially hydrolyzed polyacrylamide (HPAM) polymer is the most commonly employed water-soluble polymer in waterflooding, EOR, and well conformance treatments.^{11,12} It is obtained by a partial hydrolysis of PAM units or copolymerized of sodium acrylate and acrylamide building units.^{13,14} It is preferred in EOR because it tolerates high shear forces during reservoir flooding, comes at a low cost, and is resistant to bacterial attacks.^{13,15,16}

HPAM viscosifies the water flood, decreases the oil–water mobility ratio, and, in turn, improves the oil recovery efficiency.^{17,18} The polymer shows a strong viscosifying power in fresh water at relatively high temperatures. However, in high-salinity brine solutions, its viscosity is vastly affected by the presence of ions.¹⁹ Recent investigations are carried out on HPAM paying attention to its interaction with the anionic surfactants, such as sodium dodecyl sulfate (SDS) and sodium oleate.^{20,21} Mafi et al. studied the interaction of HPAM with SDS, and they found a possible thermodynamically stable complex with SDS, which shares the same charge of HPAM. Such a complex is stabilized via the calcium ions that bridge their interactions. HPAM is also important for the foam stability.²² Gang et al. investigated the SDS foam stability using

different degrees of hydrolysis of polyacrylamide (PAM). They claimed that, at 20% of PAM hydrolysis, the most stable foam is achieved.²² Despite these studies on HPAM, there is still a lack of information on its chain dynamics, the role of temperature, pressure, and salinity on such dynamics, and its aggregation pattern. Further, its interfacial properties are investigated on the basis of the interaction with the surfactant.²⁰

In this study, we carried out molecular dynamics (MD) simulations to investigate the degree of polymerization effect on the description of the chain dynamics of HPAM and its conformational transition from a fully extended state to a compact or coiled state. The temperature, pressure, and salinity effects were also examined. Further, the aggregation behavior of HPAM is inspected under different conditions of temperature, pressure, and salinity for two selected oligomers. The interaction of HPAM at the oil–water interface is also studied in the presence and absence of the asphaltene model, to explain the interfacial properties and response of the polymer (Figure 1).

Computational Details. All MD simulations were conducted using GROMACS 5.4.1 code²⁴ and all-atom optimized potentials for liquid simulations (OPLS-AA)^{25,26} plus extended simple point charge (SPC/E)²⁷ force fields, which are successfully described this kind of system.^{20,28} We have considered 20% of hydrolysis of PAM.²² The carboxylate

Received: January 2, 2018

Revised: February 25, 2018

Published: February 26, 2018



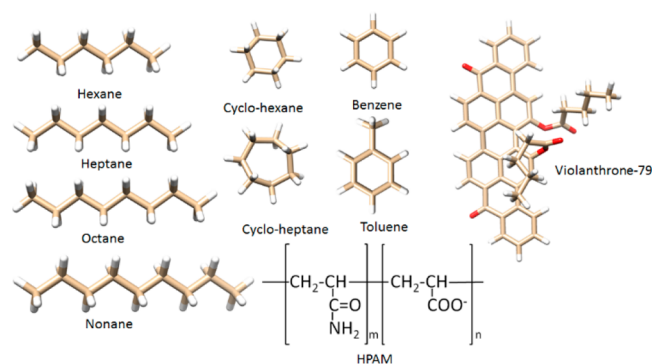


Figure 1. Molecular representation of the light-oil components, asphaltene (violanthrone-79 derivative), and the chemical structure of the HPAM polymer used in this work. The weight percentages of the light-oil components are 11.14, 14.03, 16.00, 20.71, 7.25, 13.75, 4.21, and, 12.91% for *n*-hexane, *n*-heptane, *n*-octane, *n*-nonane, cyclohexane, cycloheptane, toluene, and, benzene, respectively.²³

groups are distributed randomly and alternatively along the polymer chain. The polymer chain is considered in atactic conformation.

Systems were first energy-minimized with the steepest descent method to a convergence on the maximum force of 100 kJ mol⁻¹ nm⁻¹. The particle mesh Ewald (PME) algorithm²⁹ was applied to treat the electrostatic interactions with a cutoff of 14 Å and was used for van der Waals (VDW) and short-range electrostatic interactions. All bonds were constrained by the linear constraint solver (LINCS) algorithm.³⁰ The system was coupled to a thermal bath by a Berendsen thermostat³¹ with a time constant of 0.1 ps for equilibration and 0.5 ps for production. The pressure was controlled with a Parrinello–Rahman barostat³² with a time constants of 2 and 5 ps for equilibration and production, respectively. A time step of 2 fs was set for the simulations, and the coordinates were saved at 10 ps intervals. Trajectories are analyzed using GROMACS tools.

HPAM Chain Dynamics. Three oligomers (20-, 50-, and 100-mers) of the partially hydrolyzed PAM (HPAM20, HPAM50, and HPAM100, respectively) were generated. For the single-chain simulations, the oligomers were immersed in water boxes with a minimum distance between any atom of HPAM and the box edges to be set at 3 nm. To capture the conformational changes of HPAM, long simulations were run for 1 μs each. To examine the effect of the temperature, we carried out MD simulations at 373 K, for 300 ns. To examine the polymer properties at high salinity, MD simulations were run for 200 ns at fresh water and brine solutions using 50-mer oligomer. Two brine solutions were considered, one at the reservoir condition (brine A with *T* = 373 K, *P* = 300 bar, and salinity = 213 734 ppm) and a second at the ambient conditions keeping the same salinity (brine B with *T* = 300 K, *P* = 1 bar, and salinity = 213 734 ppm).

HPAM Aggregation. To study the polymer aggregation in fresh and brine solutions (brines A and B), a box of 16 × 16 × 16 nm³ was generated using the PACKMOL package.³⁴ Our study considered two concentrations (0.3 and 3 wt %) and two oligomers (20- and 50-mers). All of the aggregation simulations were carried out for 200 ns. The ionic composition of the brine solution is presented in Table 1.

HPAM Interfacial Properties. To inspect the interfacial properties of HPAM, we performed MD simulations on oil–

Table 1. Ionic Composition of the Brine Solution Salinity Used in This Work³³

ion	concentration (ppm)
Na ⁺	59491
Ca ²⁺	19040
Mg ²⁺	2439
SO ₄ ²⁻	350
Cl ⁻	132060
HCO ₃ ⁻	354
total dissolved solids (TDS)	213734

water systems. Light oil was modeled after Kunieda et al.²³ First, we conducted simulations on different individual systems of hexane/water, toluene/water, and light oil/water interfaces for 60 ns to calculate the interfacial tension (IFT) and density on all of the light-oil components (5 ns) to validate the OPLS force field for our system (Tables 2 and 3).

Table 2. Densities of Pure Hydrocarbons Estimated from Our MD Simulations and Compared to the Experimental Values

system	density (kg/m ³)	
	MD	experiment ^a
<i>n</i> -hexane	658	654
<i>n</i> -heptane	685	679
<i>n</i> -octane	704	698
<i>n</i> -nonane	721	714
cyclohexane	769	774
cycloheptane	798	811
benzene	874	873
toluene	871	862

^aExperimental data from ref 35.

Table 3. IFTs of Some Hydrocarbons, Light-Oil, and Water Systems Calculated from MD and Compared to the Available Data from the Experiment and Literature

system	IFT (mN/m)	
	MD	experiment
hexane	50.1 ^a (50.7 ^b)	50.5 ^c , 51.4 ^d , and 49.7 ^e
toluene	37.4 ^a (37.7 ^b)	36.0 ^f , 36.4 ^g , and 36.1 ^d
light oil	48.1 ^a (47.5 ^b)	

^aFrom this work. ^bFrom ref 23. ^cFrom ref 36. ^dFrom ref 37. ^eFrom ref 38. ^fFrom ref 39. ^gFrom ref 40.

To examine the effect of HPAM on the interfacial properties of the light oil–water system, we built four oil–water systems. The first two systems consisted of light oils with and without HPAM as used by Kunieda et al.²³ The other two systems are built with the asphaltene model as per Jian et al.⁴¹ The four systems were conducted for 100 ns.

RESULTS AND DISCUSSION

HPAM Chain Dynamics. MD simulations are employed to monitor the conformational changes of a single polymer chain using different oligomer lengths (20-, 50-, and 100-mers) in fresh water. We generated long trajectories to assess such changes (1 μs for each oligomer). The radius of gyration (*R*) and end-to-end distance (*D*) are two parameters usually used to monitor the conformational transition of macromolecules from an extended state to a compact state.^{28,42–45} The free energy

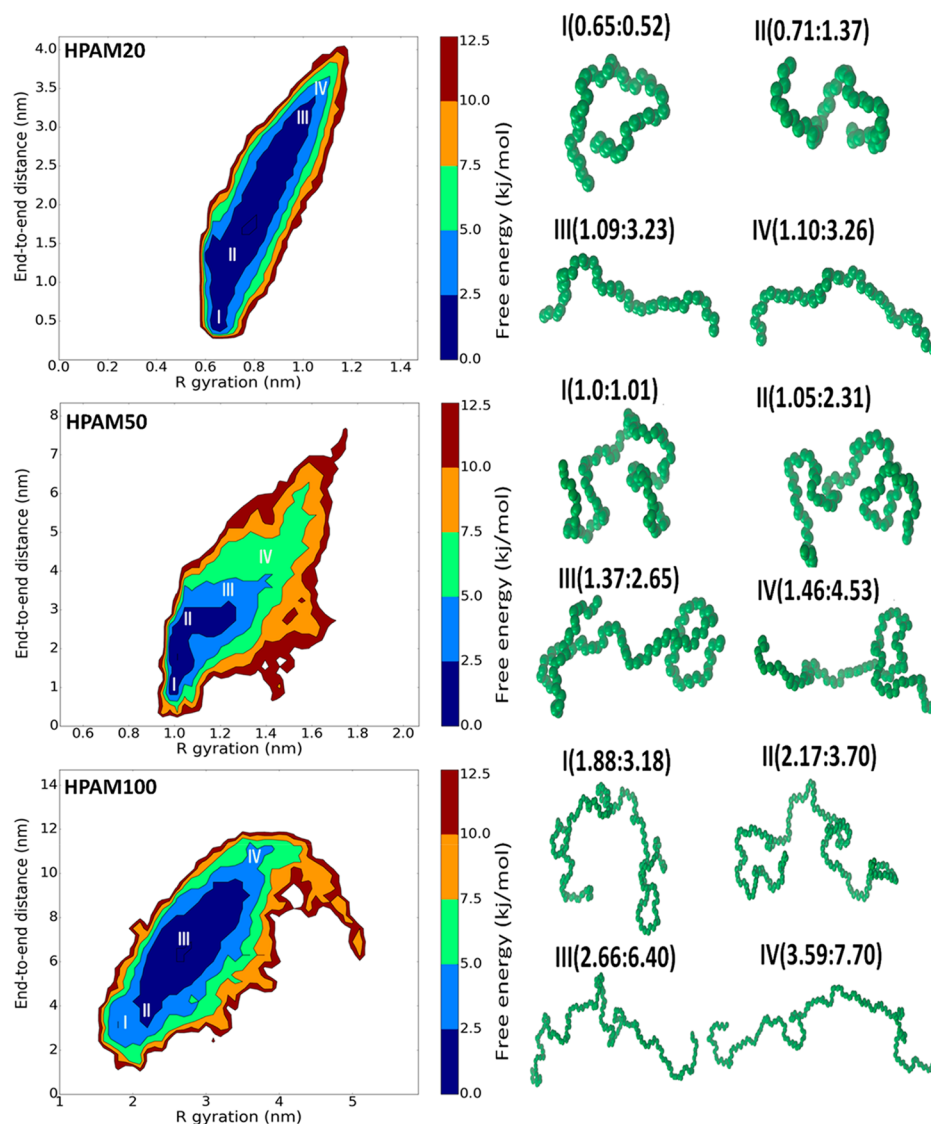


Figure 2. Left panel is the free energy (in kJ/mol) contour explored in the radius of gyration (R) and end-to-end distance (D). Right panel is snapshots representative of the explored minima. The polymer is represented in backbone green spheres.

landscape is constructed on the basis of Boltzmann probability, $G(r)$

$$G(r) = -k_B T [\ln P(r) - \ln P_{\max}(r)] \quad (1)$$

where $P(r)$ is the probability distribution of the molecular system along an order parameter or a collective variable r , P_{\max} is the maximum probability, k_B is the Boltzmann constant, and T is the simulation temperature.^{46,47} In Figure 2, the free energy contours are shown for the three considered oligomers in the radius and end-to-end distance space. The free energy landscape of the three oligomers shows high chain dynamics and a very flexible backbone. Indeed, HPAM100 samples a broad range of the collective variables R and D (from 1.65 to 3.90 nm for R and from 2.2 to 11.0 nm for D) within a small window of energy ($2kT$). A similar trend is found for HPAM50 and HPAM20 oligomers (see Figure 2). To have an idea about the structural features of the different energy basins, we have extracted snapshots from different points on the free energy landscape surface. Throughout, conformations are identified by the pair values of $R:D$ and categorized compact and coiled conformations. In Figure 2, concerning HPAM20, structures I

(0.65:0.52) and II (0.71:1.37) are considered compact, while structures III (1.09:3.23) and IV (1.10:3.26) are considered coiled. The three first structures are located in the same energy basin, although the polymer undergoes a transition from the compact to the coiled conformation within a small window of energy ($1kT$). Even more, the polymer can adopt more extended forms within $2kT$. The polymer undergoes a fast transition from a fully extended conformation (initial condition) to the compact and coiled conformations in the early equilibration stage (see Figure S2 of the Supporting Information). The same trend is noted for the two other oligomers. Indeed, the two oligomers change their conformations from compact to coiled within the thermal energy [HPAM50, structures I (1.0:1.01) and II (1.05:2.31) are compact, while structures III (1.37:2.65) and IV (1.46:4.53) are coiled; HPAM100, structures I (1.88:3.18) and II (2.17:3.70) are compact, while structures III (2.66:6.40) and IV (3.59:7.70) are coiled]. Figure S2 of the Supporting Information depicts a histogram of the radius of gyration and end-to-end distance. In this figure, HPAM20 populates the compact conformation more frequently than the other two oligomers. The population

of the compact forms is 54% for HPAM20, 38% for HPAM50, and 30% for HPAM100. Compact conformations are noted at R values not exceeding 0.8, 1.1, and 2.5 nm for HPAM20, HPAM50, and HPAM100, respectively. It seems that the HPAM20 oligomer overestimates the polymer propensity to form compact conformations compared to either HPAM50 or HPAM100.

A hairpin-like structural motif is found to be a characteristic pattern of the compact and coiled forms. This motif propagates along the polymer backbone. Obviously, longer hairpin-like motifs favor the compact form more. The compact and coiled conformations are stabilized via intra- and inter-hydrogen bonds (HB). HPAM20 has 4 intra-HB and 75 inter-HB. For the longer oligomers, the number of intra- and inter-HB that the polymer can establish increased to 16 and 170, respectively, for HPAM50 and to 24 and 355, respectively, for HPAM100. The intra-HB of these two oligomers (HPAM50 and HPAM100) undergoes a transition at 400 ns from 20 to 26 for HPAM100 and from 11 to 19 for HPAM50, which shows a kind of similar behavior between these two oligomers (see Figure S3 of the Supporting Information).

Clustering analysis was performed on the MD trajectories (see Figure S4 of the Supporting Information). A high conformational diversity of the HPAM backbone is evidenced in the root-mean-square deviation (RMSD) distribution of the clustering analysis (see Figure S5 of the Supporting Information). The width of the distribution increases as the oligomer length increases. The highest populated clusters display 68, 80, and 88% of the whole trajectory for HPAM20, HPAM50, and HPAM100, respectively. The average structure of HPAM20 has $R = 0.83$ nm and $D = 2.04$ nm. This conformation is located in the most stable energy basin and deviates by 0.51 nm from the conformation extracted from the energy basin I (see Figure 2 and Figure S4 of the Supporting Information). HPAM50 and HPAM100 are showing the same behavior. The average conformation of the highest populated cluster of HPAM50 has $R = 1.07$ nm and $D = 2.52$ nm. This conformation deviates by 0.40 nm from that of the minimum energy I, whereas HPAM100 deviates by 1.22 nm from that of the minimum energy I and has values of $R = 2.94$ nm and $D = 6.94$ nm.

To examine the temperature on the polymer chain dynamics in fresh water, we carried out simulation runs of 300 ns at high temperature (373 K), simulating the underground reservoir temperature. In Figure S6 of the Supporting Information, histograms of R and D for the three oligomers are shown. With the exception of HPAM100, the temperature seems to have no considerable effect on the HPAM structure. HPAM100 exhibited a slight shift toward a more compact form. This is in a good agreement with the experimental data reporting that HPAM maintains its viscosity at 90 °C in fresh water.⁴⁸

In addition to the temperature effect examined early for the three oligomers in fresh water, we examined the effect of salinity and pressure for HPAM50. Four runs of 300 ns simulations were carried out. Two simulations were generated at zero salinity, pressure of 1 bar, and $T = 300$ K (case 1) and $T = 373$ K (case 2). The two other runs were generated at high salinity (213 734 ppm) for varying temperatures and pressures: T and $P = 300$ K and 1 bar and 373 K and 300 bar. The aim of these simulations is to examine the effect of reservoir conditions, especially the high salinity, and separate the temperature from the pressure and salinity effects. Figure 3 shows the histogram of the end-to-end distance and radius of

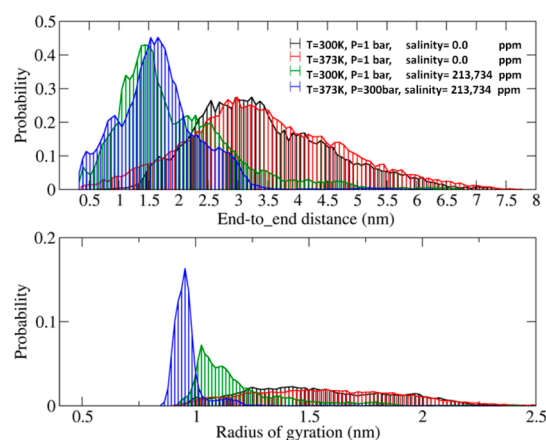


Figure 3. Histograms of the (upper panel) end-to-end distance and (lower panel) radius of gyration of HPAM50 at different conditions of temperature, pressure, and salinity.

gyration of HPAM50 oligomer at different conditions. Again, the temperature effect here is minimal, as previously noted for the longer run (1 μ s). However, at high salinity, the polymer undergoes a transition toward compact conformations. This is clear from the shift in the end-to-end distance and radius of gyration histograms. At high-salinity conditions, HPAM exhibits more compact conformations at reservoir conditions (373 K and 300 bar) than at the ambient conditions (300 K and 1 bar). This effect is evident in the radius of gyration but is absent in the case of the end-to-end distance. The conformations depicted in Figure S6 of the Supporting Information (extracted from the highest populated cluster based on the radius of gyration) show that it is possible for the polymer to have a compact conformation and relatively large end-to-end distance. Because the effect of the temperature is deemed negligible (in fresh water), one can safely assume that the effect of the reservoir conditions is mainly due to the pressure and salinity. The ability of HPAM to form a compact conformation is induced by the ion interactions, which are affected by the surrounding conditions. HPAM has a high affinity to Ca^{2+} ions compared to monovalent or Mg^{2+} ions. The interaction with calcium occurs via a direct chelation with COO^- or CONH_2 groups or indirect via water molecules (see Figure 4). The interaction with the COO^- group is much stronger than that with CONH_2 mainly as a result of the electrostatic attraction. Ca^{2+} ion interacts with COO^- directly at 0.24 nm and indirectly via water molecules at 0.43 nm. The first peak of Ca^{2+} – CONH_2 is located at 0.45 nm. The first hydration shell of the carboxylate group is located at 0.18 nm via strong hydrogen bonds, while the first hydration shell of CONH_2 is located at a larger distance of 0.3 nm. Mg^{2+} interacts with carboxylate at a shorter distance (0.20 nm) than Ca^{2+} with much less probability. Sodium and chloride display very weak affinity toward both the carboxylate and amide groups.

Our MD simulations show that HPAM has a flexible and highly dynamic backbone in fresh water and samples with compact and coiled conformation states within the thermal fluctuation limit. However, in a high brine solution, it favors the compact conformations as a result of the strong interaction with the divalent cations, mainly Ca^{2+} (see Figure S7 of the Supporting Information). The ionic effect on the polymer conformation is unexpected, especially the divalent cations, such as Ca^{2+} and Mg^{2+} , which share the same charge, and there is a little difference in the ionic size. It is understandable that

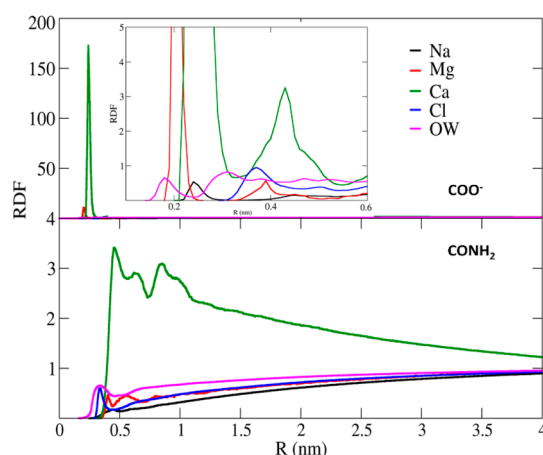


Figure 4. RDF between HPAM (COO^- and CONH_2) and ions as well as water. A zoom-in for the RDF between ions and the COO^- group is shown in the upper panel at the reservoir conditions ($T = 373$ K, $P = 300$ bar, and salinity = 213 734 ppm).

Ca^{2+} and Mg^{2+} with two positive charges bind to HPAM stronger than Na^+ with one positive charge. However, we cannot explain the binding preference of Ca^{2+} and Mg^{2+} based on the electrostatic model or the ionic size differences. Even if we consider the ionic size, Mg^{2+} does have a charge density higher than that of Ca^{2+} because the latter is larger in size than the former. This implies that Mg^{2+} should bind more tightly to HPAM than Ca^{2+} , which is not observed in our simulation.

The binding preference of Ca^{2+} and Mg^{2+} can be explained by considering the ionic dehydration free energy. Indeed, Mg^{2+} has a dehydration free energy of 1830 kJ/mol, while Ca^{2+} has 1505 kJ/mol. Mg^{2+} is difficult to dehydrate (325 kJ/mol dehydration free energy difference), whereas Ca^{2+} is easier.⁴⁹ This implies that Mg^{2+} ions prefer to bind to water than HPAM. In Figure S8 of the Supporting Information, we have calculated RDF between the considered ions and water in brine A solution and fresh water. It is clearly shown that, regardless of brine or fresh water, Mg^{2+} does show higher affinity toward water molecules than Ca^{2+} ions.

The HPAM–ion interactions drive the thermodynamic equilibrium between the compact and coiled conformations toward the compact conformation. These results are in agreement with the experimental studies on how salts affect the rheological properties of HPAM. Samanta et al.¹⁹ claimed that the salts reduce the polymer viscosity by reducing its hydrodynamic size. As a final remark on the single-chain simulations, the short oligomers (HPAM20) overestimate the tendency of the polymer to form compact conformations.

HPAM Nanoscale Aggregation. MD simulations were conducted for 200 ns on HPAM under three different conditions. One case ran in fresh water at ambient conditions ($T = 300$ K, $P = 1$ bar, and salinity = 0 ppm). The two other cases targeted HPAM in high-salinity brine solutions at reservoir conditions (brine A with $T = 373$ K, $P = 300$ bar, and salinity = 213 734 ppm) and at ambient conditions (brine B with $T = 300$ K, $P = 1$ bar, and salinity = 213 734 ppm). We excluded the HPAM100 oligomer from the study because of its high computational cost. Five chains of HPAM20 were placed in a $16 \times 16 \times 16$ nm³ box. This corresponds to a concentration of 0.04 mol/L or 0.3 wt %. Initial simulation runs showed that this concentration is too low to generate any meaningful statistical results on the aggregation pattern of the

polymer (see Figure S9 of the Supporting Information). As such, we ran the simulations using a 10-fold increase in this concentration (3 wt %). This corresponds to 50 chains of HPAM20 and 20 chains of HPAM50. The aggregation pattern of the polymer is quickly stabilized within 40 ns (see Figure 5).

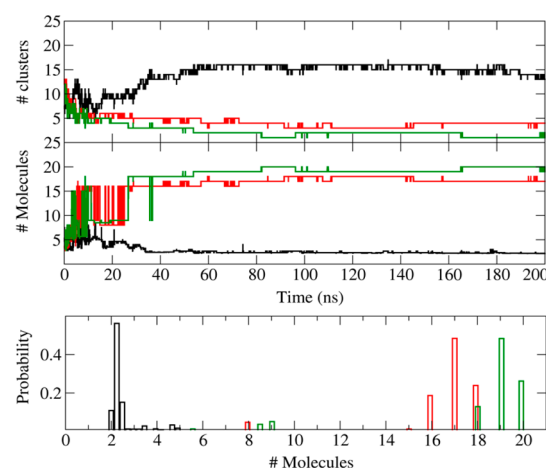


Figure 5. Upper panel is showing the time evolution of the average cluster size and number of cluster of HPAM50 at a concentration of 3 wt %: (black line) fresh water with $T = 300$ K, $P = 1$ bar, and salinity = 0.0 ppm, (green line) brine A with $T = 373$ K, $P = 1$ bar, and salinity = 213 734 ppm, and (red line) brine B with $T = 300$ K, $P = 300$ bar, and salinity = 213 734 ppm. Lower panel is the histogram of the aggregation size for the above three mentioned conditions.

Obviously, salinity, reservoir temperature, and pressure play important roles in defining the aggregation pattern of the polymer. Indeed, in the fresh water case, the polymer is completely soluble with only very tiny aggregates of around 2 molecules in size (black line in Figure 5). At high-salinity cases, HPAM50 is aggregating with an average size of 17 and 19 molecules under brine B (red line in Figure 5) and brine A (green line in Figure 5) conditions, respectively. These large-size aggregates in the two brine cases account for up to 85 and 95% of the total number of molecules in solution. Accordingly, there is a high tendency of aggregation under these conditions. Reservoir conditions were found to have a slight impact on the size of aggregation compared to the ambient conditions. The major factor controlling the aggregation size is the salt effect. The same trend of the salinity effect is found for HPAM20. However, it overestimates the polymer solubility, and its aggregates are of a smaller size (see Figure S10 of the Supporting Information). The highest populated aggregates of HPAM20 in brine A are of about 13 and 17 molecules, while in brine B, the biggest aggregate is of 7 molecules in size. These aggregates account for up to 26, 34, and 14% of the total molecules in brines A and B, respectively.

Figures S11 and S12 of the Supporting Information present the chain average radius of gyration and end-to-end distance of HPAM20 and HPAM50 oligomers. In brine A, the majority of HPAM50 chains adopt a compact conformation and a coiled conformation in brine B. Both forms are populated in fresh water. For HPAM20, on the other hand, samples have more coiled conformations and the histograms in the three solutions (brine A, brine B, and fresh water) overlap. The shape of the nanosize aggregates of HPAM50 is wire-like for HPAM50 and near spherical for HPAM20 (see Figure S13 of the Supporting Information). Overall, HPAM is found to have a high

propensity to aggregate and form compact conformations in the presence of ions. The use of the HPAM20 oligomer is underestimating the tendency of the HPAM polymer to aggregate in either brine A or brine B solutions.

To obtain a deeper picture of the interaction between the counterions (Na^+ , Ca^{2+} , Mg^{2+} , and Cl^-) and HPAM functional groups (COO^- and CONH_2), the radial distribution function (RDF) is calculated. Results reported in Figure 6 and Figure

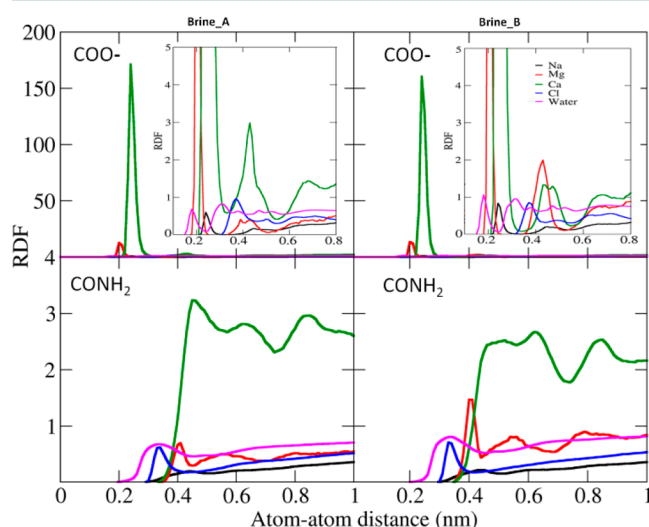


Figure 6. RDF between oxygen and nitrogen atoms of COO^- and CONH_2 groups and Na^+ , Mg^{2+} , Ca^{2+} , Cl^- , and oxygen of water (OW) atoms in brine A and B solutions. A zoom-in for the COO^- group is also shown. The results are reported for HPAM50 at 3 wt % concentration.

S14 of the Supporting Information show that HPAM has a high tendency to interact with calcium ions but a lesser affinity toward the other ions in the brine. Also, the affinity of the COO^- group to the ions is much higher than that of CONH_2 . In general, the interaction of the COO^- group with the divalent is much stronger than with the monovalent ions. The interactions of the divalent cations occur at two main peaks for both calcium and magnesium ions: the strong peaks are located at 0.20 nm (Mg^{2+}) and 0.24 nm (Ca^{2+}), and the weaker peaks are located at 0.39 nm (Mg^{2+}) and 0.43 nm (Ca^{2+}). On the other hand, the interactions of monovalent ions with the carboxylate group can be identified with the peaks located at 0.24 nm (Na^+) and 0.37 nm (Cl^-). Water molecules are located at 0.18 and 0.30 nm via hydrogen bonds. Chloride ions are located between the two calcium peaks and after the second water layer. The temperature does not seem to affect the first ionic layer around COO^- and CONH_2 groups. However, at the second loose ionic layer, it weakens the interaction of HPAM with Ca^{2+} located at 0.43 nm and strengthens that with Mg^{2+} at 0.39 nm. The temperature slightly weakens the water interaction at the two layers and the chloride ion affinity as well. The interactions with the CONH_2 group are located at a larger distance and are much weaker than those with the COO^- group. Ca^{2+} ions still display the highest affinity (among the remaining ions and water molecules) toward the CONH_2 group.

To quantify the interaction of HPAM with ions, we estimated the potential mean force (PMF) using eq 2^{50,51}

$$\text{PMF} = -k_B T \ln(\text{RDF}) \quad (2)$$

where k_B is the Boltzmann constant, T is the simulation temperature, and RDF is the radial distribution function between the ion and COO^- group. It is evident from Figure 7

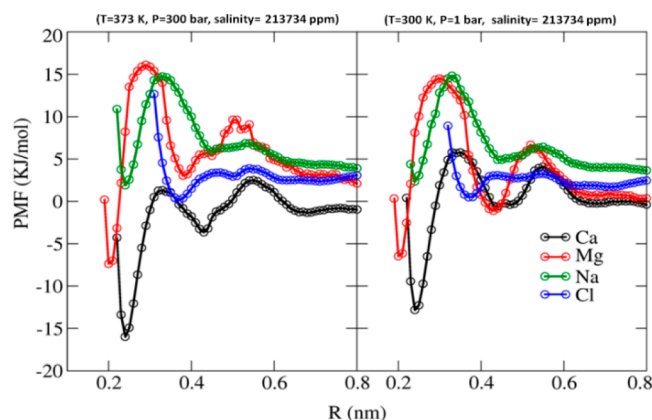


Figure 7. PMF of the carboxylate-ion interaction estimated using eq 2 in brines A and B.

that Ca^{2+} displays the most thermodynamically stable complex among all of the other ions in both brine solutions. For brine A, the first minimum appeared at 0.24 nm with pairing free energy of -15.97 kJ/mol, which corresponds to the direct interaction between Ca^{2+} and the COO^- group. The second energy minimum appeared at 0.43 nm and -3.66 kJ/mol, which corresponds to indirect interactions via water molecules. The first peak of the free energy profile appeared at 0.33 nm and 1.12 kJ/mol, which corresponds to the barrier for binding/dissociation of the Ca^{2+} – COO^- ion pair complex. The Ca^{2+} – COO^- pairing energy (-15.97 kJ/mol) is in good agreement with the pairing free energy of Ca^{2+} with the carbonate anion from the experiment (-17.2 kJ/mol)⁵² and metadynamic simulation (-18.8 kJ/mol).⁵³ The binding of Ca^{2+} ion to COO^- has a small barrier of 4.78 kJ/mol, while for dissociation is much high (17.10 kJ/mol). The pairing of Ca^{2+} – COO^- in brine B has the same trend as in brine A. Indeed, in brine B, the barriers of binding/dissociation are $6.37/18.2$ kJ/mol and located at 0.35 nm, while the two minima are located at -12.82 and -0.61 kJ/mol. The other ions display very small affinity toward the COO^- group and much less toward the CONH_2 group. The temperature boosts the barrier of binding and decreases the barrier of dissociation, which leads to small changes of the accumulated calcium ions around COO^- groups. The other ions either have high energetic barriers, such as Mg^{2+} , or form unstable complexes, such as Na^+ and Cl^- .

The strong interaction between HPAM and ions implies that HPAM does not tolerate the reservoir conditions of high salinity and aggregates quickly. In addition, HPAM should suffer from the loss problem as a result of its adsorption on the rock surface.

HPAM Interfacial Properties. Previously, we analyzed the polar interactions of HPAM with its surrounding environment and how it impacts the polymer chain dynamics and its aggregation pattern. The interaction of HPAM and the anionic surfactant (SDS) was recently discussed in the literature, highlighting the importance of this interaction on the interfacial properties of the surfactants.²⁰ Here, we shed light on the HPAM role on the interfacial properties of the oil–water system, notably the IFT in the absence of surfactants. To do so, we carried out MD simulations on oil–water systems. In the

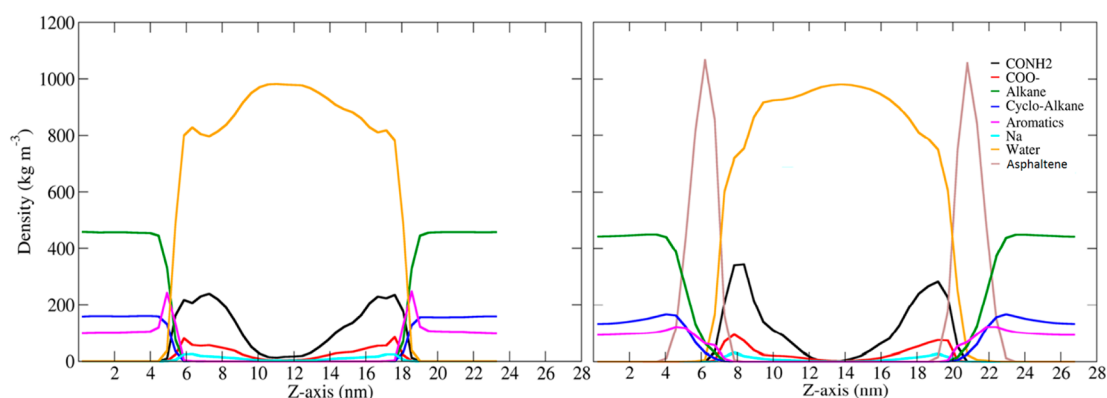


Figure 8. Partial density profile of COO^- , CONH_2 , water, sodium ions, and oil components along the z axis of the simulation box.

water phase, HPAM50 has a concentration of 3 wt % placed as a thin film at the interface. This is because the interfacial properties are linked to the surface concentration rather than the bulk.⁴¹ Two oil models are simulated. The first is based on the light oil widely used in the literature.²³ The second model is comprised of a thin film of asphaltene used to monitor the role of the HPAM–asphaltene interaction on the IFT. To minimize the initial condition effects, we simulated the oil–water systems in the presence of HPAM for 100 ns, then removed HPAM, and followed the simulation for another 100 ns. The IFT of the light-oil–water system averaged over the last 50 ns is 47.4 mN/m, which is in good agreement with the previously reported values.²³ In the presence of HPAM, IFT has just decreased to 45.2 mN/m only. In the case of a thin film of asphaltene, no significant role of HPAM on the IFT of the oil–water system was observed. Indeed, in the absence of HPAM, the heavy oil–water system has an IFT of 35.8 mN/m, which again in good agreement with previous studies on the role of asphaltene on the IFT.^{41,54} HPAM increased the IFT value by almost 2 units (37.7 mN/m). Such small changes are in the limit of IFT fluctuations estimated from MD.^{55,56} Further, in Figure 8, the partial density along the z axis (perpendicular to the interface) is shown for the system components. The interaction of HPAM with either the heavy or light oil is well-screened by water. Moreover, the RDF shown in Figure 9 shows that there are no interactions between HPAM monomers and the oil compo-

nents, even with the asphaltene, which is polar in nature. These simulated interfaces provide evidence of the spectator role of HPAM on the interfacial properties of the oil–water system in the absence of surfactants. This result is in agreement with the early reported experimental data.⁵⁷

CONCLUSION

We carried out MD simulations to examine the HPAM chain dynamics, its aggregation, and its interfacial properties. Results reported here showed that HPAM has a very flexible backbone and a high conformational diversity. In fresh water, HPAM populates compact and coiled conformations within the thermal energy limit with very little impact of the temperature on its dynamics. In brine solutions, the flexibility of HPAM does not tolerate the high salinity of the “reservoir environment” and favors more compact conformations driven by the ion interactions, especially with calcium ions. It exhibits a high tendency to form large-size aggregates in the presence of ions (brine solutions), while it is completely soluble in fresh water.

HPAM–ion interactions has an important effect on HPAM properties (chain dynamics and aggregation), especially the Ca^{2+} ions. The latter has unexpected behavior compared to Mg^{2+} , with both of them sharing the same charge. We can only explain such a divergent binding preference using the dehydration free energy concept. Mg^{2+} ions are difficult to dehydrate and prefer to tightly bind to water rather than to HPAM. In contrast, Ca^{2+} ions are easier to dehydrate, which make them preferably bind to HPAM than to water. HPAM–ion interactions imply that HPAM does not tolerate the high salinity of reservoir conditions. Further, in carbonate reservoirs, HPAM should suffer from the adsorption on the rock surface.

We observed that short oligomers overestimate both the tendency of the polymer to form compact conformations and the solubility in brine solutions. Thus, we recommend using the 50-mer oligomer to simulate HPAM properties because it forms a good compromise between accuracy and computational cost. Finally, we investigated the interfacial properties of HPAM. Two oil–water systems were considered (light and heavy oils). In both cases, HPAM had little impact on the IFT of the oil–water systems. It is quickly screened by water molecules, although it has been shown that it impacts the interfacial properties of surfactants.²⁰ This is induced by the divalent cations, which mediated its interaction with the ionic part of the surfactant.

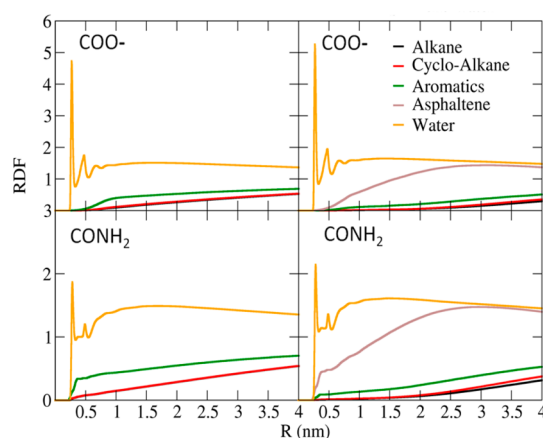


Figure 9. RDF between oxygen and nitrogen atoms of COO^- and CONH_2 groups and Na^+ , Mg^{2+} , Ca^{2+} , Cl^- , and OW atoms. The left-hand side is for the light-oil–water system, and the right-hand side is for the heavy-oil–water system.

■ ASSOCIATED CONTENT

■ Supporting Information

The Supporting Information is available free of charge on the ACS Publications website at DOI: [10.1021/acs.energyfuels.8b00010](https://doi.org/10.1021/acs.energyfuels.8b00010).

Dynamic control of the radius of gyration and end-to-end distance, their histograms, analysis of the hydrogen bonds of the three oligomers, clustering analysis, temperature effect on the radius of gyration and end-to-end distance, and aggregation analysis (PDF)

■ AUTHOR INFORMATION

Corresponding Author

*E-mail: abdelaizeim@kfupm.edu.sa.

ORCID

Safwat Abdel-Azeim: [0000-0001-8611-1251](https://orcid.org/0000-0001-8611-1251)

Notes

The authors declare no competing financial interest.

■ ACKNOWLEDGMENTS

The authors thank the Supercomputer Shaheen at King Abdullah University of Science & Technology (KAUST) in Thuwal, Saudi Arabia, for the permission to use its computational resources.

■ REFERENCES

- (1) Siggel, L.; Santa, M.; Hansch, M.; Nowak, M.; Ranft, M.; Weiss, H.; Hajnal, D.; Schreiner, E.; Oetter, G.; Tinsley, J. A New Class of Viscoelastic Surfactants for Enhanced Oil Recovery. *Proceedings of the SPE Improved Oil Recovery Symposium*; Tulsa, OK, April 14–18, 2012; DOI: [10.2118/153969-MS](https://doi.org/10.2118/153969-MS).
- (2) Morvan, M.; Moreau, P.; Degre, G.; Leng, J.; Masselon, C.; Bouillot, J.; Zaitoun, A. New Viscoelastic Fluid for Chemical EOR. *Proceedings of the SPE International Symposium on Oilfield Chemistry*; The Woodlands, TX, April 20–22, 2009; DOI: [10.2118/121675-MS](https://doi.org/10.2118/121675-MS).
- (3) Sandra, I.; Sandra, R. Global Oil Reserves—1: Recovery Factors Leave Vast Target for EOR Technologies. *Oil Gas J.* **2007**, 105 (41), 44.
- (4) Lakatos, I. Role of Chemical IOR/EOR Methods in the 21st Century. *Proceedings of the 18th World Petroleum Congress*; Johannesburg, South Africa, Sept 25–29, 2005.
- (5) Alvarado, V.; Manrique, E. Enhanced Oil Recovery: An Update Review. *Energies* **2010**, 3 (9), 1529–1575.
- (6) Al-Adasani, A.; Bai, B. Recent Developments and Updated Screening Criteria of Enhanced Oil Recovery Techniques. *Proceedings of the International Oil and Gas Conference and Exhibition in China*; Beijing, China, June 8–10, 2010; DOI: [10.2118/130726-MS](https://doi.org/10.2118/130726-MS).
- (7) Thomas, S. Enhanced Oil Recovery—an Overview. *Oil Gas Sci. Technol.* **2008**, 63 (1), 9–19.
- (8) Wei, B.; Romero-Zerón, L.; Rodrigue, D. Oil Displacement Mechanisms of Viscoelastic Polymers in Enhanced Oil Recovery (EOR): A Review. *J. Pet. Explor. Prod. Technol.* **2014**, 4 (2), 113–121.
- (9) Hirasaki, G. J.; Miller, C. A.; Puerto, M. Recent Advances in Surfactant EOR. *Proceedings of the SPE Annual Technical Conference and Exhibition*; Denver, CO, Sept 21–24, 2008; DOI: [10.2118/115386-MS](https://doi.org/10.2118/115386-MS).
- (10) Kamal, M. S.; Hussein, I. A.; Sultan, A. S. Review on Surfactant Flooding: Phase Behavior, Retention, IFT, and Field Applications. *Energy Fuels* **2017**, 31 (8), 7701–7720.
- (11) Morgan, S. E.; McCormick, C. L. Water-Soluble Polymers in Enhanced Oil Recovery. *Prog. Polym. Sci.* **1990**, 15 (1), 103–145.
- (12) Olajire, A. A. Review of ASP EOR (Alkaline Surfactant Polymer Enhanced Oil Recovery) Technology in the Petroleum Industry: Prospects and Challenges. *Energy* **2014**, 77, 963–982.
- (13) Wever, D. A. Z.; Picchioni, F.; Broekhuis, A. A. Polymers for Enhanced Oil Recovery: A Paradigm for Structure–property Relationship in Aqueous Solution. *Prog. Polym. Sci.* **2011**, 36 (11), 1558–1628.
- (14) Sheng, J. J.; Leonhardt, B.; Azri, N. Status of Polymer-Flooding Technology. *J. Can. Pet. Technol.* **2015**, 54 (02), 116–126.
- (15) Chen, Q.; Wang, Y.; Lu, Z.; Feng, Y. Thermoviscosifying Polymer Used for Enhanced Oil Recovery: Rheological Behaviors and Core Flooding Test. *Polym. Bull.* **2013**, 70 (2), 391–401.
- (16) Xia, H.; Wang, D.; Wu, J.; Kong, F. Elasticity of HPAM Solutions Increases Displacement Efficiency under Mixed Wettability Conditions. *Proceedings of the SPE Asia Pacific Oil and Gas Conference and Exhibition*; Perth, Australia, Oct 18–20, 2004; DOI: [10.2118/88456-MS](https://doi.org/10.2118/88456-MS).
- (17) Sorbie, K. S. *Polymer-Improved Oil Recovery*; Blackie and Son, Ltd.: Glasgow, U.K., 1991.
- (18) Hou, J.; Liu, Z.; Zhang, S.; Yue, X.; Yang, J. The Role of Viscoelasticity of Alkali/Surfactant/Polymer Solutions in Enhanced Oil Recovery. *J. Pet. Sci. Eng.* **2005**, 47 (3), 219–235.
- (19) Samanta, A.; Bera, A.; Ojha, K.; Mandal, A. Effects of Alkali, Salts, and Surfactant on Rheological Behavior of Partially Hydrolyzed Polyacrylamide Solutions. *J. Chem. Eng. Data* **2010**, 55 (10), 4315–4322.
- (20) Mafi, A.; Hu, D.; Chou, K. C. Complex Formations between Surfactants and Polyelectrolytes of the Same Charge on a Water Surface. *Langmuir* **2017**, 33 (32), 7940–7946.
- (21) Xin, X.; Xu, G.; Gong, H.; Bai, Y.; Tan, Y. Interaction between Sodium Oleate and Partially Hydrolyzed Polyacrylamide: A Rheological Study. *Colloids Surf., A* **2008**, 326 (1), 1–9.
- (22) Li, C.; Zhang, T.; Ji, X.; Wang, Z.; Sun, S.; Hu, S. Effect of Ca 2+ /Mg 2+ on the Stability of the Foam System Stabilized by an Anionic Surfactant: A Molecular Dynamics Study. *Colloids Surf., A* **2016**, 489, 423–432.
- (23) Kunieda, M.; Nakaoka, K.; Liang, Y.; Miranda, C. R.; Ueda, A.; Takahashi, S.; Okabe, H.; Matsuoka, T. Self-Accumulation of Aromatics at the Oil–Water Interface through Weak Hydrogen Bonding. *J. Am. Chem. Soc.* **2010**, 132 (51), 18281–18286.
- (24) Hess, B.; Kutzner, C.; Van Der Spoel, D.; Lindahl, E. GROMACS 4: Algorithms for Highly Efficient, Load-Balanced, and Scalable Molecular Simulation. *J. Chem. Theory Comput.* **2008**, 4 (3), 435–447.
- (25) Jorgensen, W. L.; Tirado-Rives, J. The OPLS [Optimized Potentials for Liquid Simulations] Potential Functions for Proteins, Energy Minimization for Crystals of Cyclic Peptides and Crambin. *J. Am. Chem. Soc.* **1988**, 110 (6), 1657–1666.
- (26) Jorgensen, W. L.; Maxwell, D. S.; Tirado-Rives, J. Development and Testing of the OPLS All-Atom Force Field on Conformational Energetics and Properties of Organic Liquids. *J. Am. Chem. Soc.* **1996**, 118 (45), 11225–11236.
- (27) Berendsen, H. J. C.; Grigera, J. R.; Straatsma, T. P. The Missing Term in Effective Pair Potentials. *J. Phys. Chem.* **1987**, 91 (24), 6269–6271.
- (28) Bořan, V.; Ustach, V.; Faller, R.; Leonhard, K. Direct Phase Equilibrium Simulations of NIPAM Oligomers in Water. *J. Phys. Chem. B* **2016**, 120 (13), 3434–3440.
- (29) Darden, T.; York, D.; Pedersen, L. Particle Mesh Ewald: An N-Log (N) Method for Ewald Sums in Large Systems. *J. Chem. Phys.* **1993**, 98 (12), 10089–10092.
- (30) Hess, B.; Bekker, H.; Berendsen, H. J.; Fraaije, J. G. LINCS: A Linear Constraint Solver for Molecular Simulations. *J. Comput. Chem.* **1997**, 18 (12), 1463–1472.
- (31) Lemak, A. S.; Balabaev, N. K. On the Berendsen Thermostat. *Mol. Simul.* **1994**, 13 (3), 177–187.
- (32) Martoňák, R.; Laio, A.; Parrinello, M. Predicting Crystal Structures: The Parrinello-Rahman Method Revisited. *Phys. Rev. Lett.* **2003**, 90 (7), 075503.
- (33) Mahmoud, M. A.; Abdelgawad, K. Z. Chelating-Agent Enhanced Oil Recovery for Sandstone and Carbonate Reservoirs. *SPE J.* **2015**, 20 (03), 483–495.

- (34) Martínez, L.; Andrade, R.; Birgin, E. G.; Martínez, J. M. PACKMOL: A Package for Building Initial Configurations for Molecular Dynamics Simulations. *J. Comput. Chem.* **2009**, *30* (13), 2157–2164.
- (35) Lemmon, E. W.; McLinden, M. O.; Friend, D. G. Thermophysical Properties of Fluid Systems. In *NIST Chemistry WebBook, NIST Standard Reference Database* 69; Linstrom, P. J., Mallard, W. G., Eds.; National Institute of Standards and Technology (NIST): Gaithersburg, MD, 2005.
- (36) Rehfeld, S. J. Adsorption of Sodium Dodecyl Sulfate at Various Hydrocarbon-Water Interfaces. *J. Phys. Chem.* **1967**, *71* (3), 738–745.
- (37) Goebel, A.; Lunkenheimer, K. Interfacial Tension of the Water/*n*-Alkane Interface. *Langmuir* **1997**, *13* (2), 369–372.
- (38) Donahue, D. J.; Bartell, F. E. The Boundary Tension at Water-Organic Liquid Interfaces. *J. Phys. Chem.* **1952**, *56* (4), 480–484.
- (39) Dabros, T.; Yeung, A.; Masliyah, J.; Czarnecki, J. Emulsification through Area Contraction. *J. Colloid Interface Sci.* **1999**, *210* (1), 222–224.
- (40) Moran, K.; Yeung, A.; Masliyah, J. Measuring Interfacial Tensions of Micrometer-Sized Droplets: A Novel Micromechanical Technique. *Langmuir* **1999**, *15* (24), 8497–8504.
- (41) Jian, C.; Poopari, M. R.; Liu, Q.; Zerpa, N.; Zeng, H.; Tang, T. Reduction of Water/Oil Interfacial Tension by Model Asphaltenes: The Governing Role of Surface Concentration. *J. Phys. Chem. B* **2016**, *120* (25), 5646–5654.
- (42) Mansfield, K. F.; Theodorou, D. N. Molecular Dynamics Simulation of a Glassy Polymer Surface. *Macromolecules* **1991**, *24* (23), 6283–6294.
- (43) Wang, X.; Qiu, X.; Wu, C. Comparison of the Coil-to-Globule and the Globule-to-Coil Transitions of a Single Poly (N-Isopropylacrylamide) Homopolymer Chain in Water. *Macromolecules* **1998**, *31* (9), 2972–2976.
- (44) Minagawa, K.; Matsuzawa, Y.; Yoshikawa, K.; Khokhlov, A. R.; Doi, M. Direct Observation of the Coil-Globule Transition in Dna Molecules. *Biopolymers* **1994**, *34* (4), 555–558.
- (45) Deng, S.; Arinstein, A.; Zussman, E. Size-Dependent Mechanical Properties of Glassy Polymer Nanofibers via Molecular Dynamics Simulations. *J. Polym. Sci., Part B: Polym. Phys.* **2017**, *55* (6), 506–514.
- (46) Altis, A.; Otten, M.; Nguyen, P. H.; Hegger, R.; Stock, G. Construction of the Free Energy Landscape of Biomolecules via Dihedral Angle Principal Component Analysis. *J. Chem. Phys.* **2008**, *128* (24), 245102.
- (47) Abdel-Azeim, S.; Oliva, R.; Chermak, E.; De Cristofaro, R.; Cavallo, L. Molecular Dynamics Characterization of Five Pathogenic Factor X Mutants Associated with Decreased Catalytic Activity. *Biochemistry* **2014**, *53* (44), 6992–7001.
- (48) Ryles, R. G. Chemical Stability Limits of Water-Soluble Polymers Used in Oil Recovery Processes. *SPE Reservoir Eng.* **1988**, *3* (01), 23–34.
- (49) Marcus, Y. A Simple Empirical Model Describing the Thermodynamics of Hydration of Ions of Widely Varying Charges, Sizes, and Shapes. *Biophys. Chem.* **1994**, *51* (2–3), 111–127.
- (50) Ghosh, T.; García, A. E.; Garde, S. Molecular Dynamics Simulations of Pressure Effects on Hydrophobic Interactions. *J. Am. Chem. Soc.* **2001**, *123* (44), 10997–11003.
- (51) Yan, H.; Guo, X.-L.; Yuan, S.-L.; Liu, C.-B. Molecular Dynamics Study of the Effect of Calcium Ions on the Monolayer of SDC and SDSn Surfactants at the Vapor/Liquid Interface. *Langmuir* **2011**, *27* (10), 5762–5771.
- (52) De Visscher, A.; Vanderdeelen, J. IUPAC-NIST Solubility Data Series. 95. Alkaline Earth Carbonates in Aqueous Systems. Part 2. Ca. *J. Phys. Chem. Ref. Data* **2012**, *41* (2), 023105.
- (53) Raiteri, P.; Demichelis, R.; Gale, J. D. Thermodynamically Consistent Force Field for Molecular Dynamics Simulations of Alkaline-Earth Carbonates and Their Aqueous Speciation. *J. Phys. Chem. C* **2015**, *119* (43), 24447–24458.
- (54) Mikami, Y.; Liang, Y.; Matsuo, T.; Boek, E. S. Molecular Dynamics Simulations of Asphaltenes at the Oil–water Interface: From Nanoaggregation to Thin-Film Formation. *Energy Fuels* **2013**, *27* (4), 1838–1845.
- (55) Alejandre, J.; Tildesley, D. J.; Chapela, G. A. Molecular Dynamics Simulation of the Orthobaric Densities and Surface Tension of Water. *J. Chem. Phys.* **1995**, *102* (11), 4574–4583.
- (56) Rivera, J. L.; McCabe, C.; Cummings, P. T. Molecular Simulations of Liquid–Liquid Interfacial Properties: Water–*n*-Alkane and Water–Methanol–*n*-Alkane Systems. *Phys. Rev. E: Stat. Phys., Plasmas, Fluids, Relat. Interdiscip. Top.* **2003**, *67* (1), 011603.
- (57) Pope, G. A.; Tsaur, K.; Schechter, R. S.; Wang, B. The Effect of Several Polymers on the Phase Behavior of Micellar Fluids. *SPEJ, Soc. Pet. Eng. J.* **1982**, *22* (06), 816–830.